Politecnico di Milano

Dipartimento di Ingegneria Aerospaziale

Direct numerical simulation of turbulent Taylor–Couette flow

Davide Pirró & Maurizio Quadrio

Scientific Report
DIA-SR 06-11

2006

.

Scientific Report DIA-SR 06-11

Published by
Politecnico di Milano, Dipartimento di Ingegneria Aerospaziale
Campus Bovisa
via La Masa 34
20156 Milano, Italy

Printed in Italy
December 2006

Direct Numerical Simulation of turbulent Taylor–Couette flow

Davide Pirrò, Maurizio Quadrio [a,*]

[a] *Dipartimento di Ingegneria Aerospaziale Politecnico di Milano - Italy*

Abstract

The Direct Numerical Simulation (DNS) of the Couette–Taylor flow in the fully turbulent regime is described. Following Quadrio & Luchini (Eur. J. Mech. B / Fluids, **21**, 413–427, 2002), the incompressible Navier–Stokes equations in cylindrical coordinates are transformed into two scalar equations for the radial component of velocity and vorticity vectors, with the divergence-free condition accounted for implicitely. The spatial discretization is mixed, with spectral schemes in the homogeneous directions, and finite differences in the radial direction. Main improvements are the use of fourth-order, compact explicit finite-differences schemes, and an innovative parallel strategy designed to obtain high parallel performance on a distributed/shared memory machine made by personal computers. A computationally demanding DNS is then carried out to simulate for the first time the Taylor–Couette flow in the turbulent regime. Statistical quantities are computed to complement the existing experimental information available for the turbulent Taylor–Couette flow, with a view to compare it to planar, pressure-driven turbulent flow at the same value of the Reynolds number. The main source for differences in flow statistics between plane and curved-wall flows is attributed to the presence of large-scale vortical structures generated by curvature effects.

1. Introduction

The flow in the gap between coaxial rotating cylinders, known as the Couette–Taylor flow (CTF hereinafter), is among the most investigated problems in fluid mechanics (see [1] for a recent overview), owing to its engineering applications [2], as well as to its relevance as

* Corresponding author. Address: Dipartimento di Ingegneria Aerospaziale del Politecnico di Milano - via La Masa 34 - 20156 Milano - Italy

Email addresses: davide.pirro@polimi.it, maurizio.quadrio@polimi.it (Davide Pirrò, Maurizio Quadrio).

prototypical flow in the study of transition to turbulence and of fully-developed turbulent flows over streamwise-curved surfaces.

Many experimental studies have dealt with the instabilities developed by the CTF when the value of the Reynolds number is increased such that the laminar regime is taken over by a sequence of bifurcations, eventually leading to chaotic behavior. Less is known about the turbulent regime, since a smaller number of laboratory experiments and essentially no Direct Numerical Simulation (DNS) studies are available. The lack of DNS studies can be ascribed – at least in part – to the difficulties of implementing an efficient method for the numerical solution of the incompressible Navier–Stokes equations in cylindrical geometries, as well as to the computational demand of such a simulation in turbulent regime. A satisfactory quantitative description of the turbulent CTF, leveraging the full space-time information that could be made available by a DNS, is as yet missing.

In this paper a numerical method for the DNS of the Navier–Stokes in cylindrical coordinates is presented, which is designed to compute the Couette–Taylor flow in the turbulent regime. The method relies on the strategy developed by Quadrio & Luchini [3] for the DNS of a turbulent flow in an annular pipe: the main enhancements used here since that paper are a much better spatial accuracy, and the ability of the code to exploit parallel computing on commodity hardware. The capabilities of the cylindrical Navier–Stokes solver are thus made comparable to those of its cartesian counterpart, recently described in [4].

The newly developed numerical method is then used to carry out what we believe is the first DNS of the turbulent Couette–Taylor flow. We shall focus on a so-called small-gap geometry, identical to that considered by Andereck, Liu & Swinney [5]. In the analysis of the results, emphasis will be placed on the assessment of low-order flow statistics, and on some theoretical issues that concern turbulent flows with wall curvature. As described at length in the review paper [6] by Patel & Sotiropoulos, this might considerably impact the modeling of turbulent flows, as well as on current experimental practices. For example, when measuring the skin friction in a turbulent flow over a curved wall, one often resorts to methods (like the Clauser plot) which imply the validity of the law of the wall, and which require moreover the numerical values of its parameters (i.e. the slope of the logarithmic part of the profile, given by the inverse of the von Kármán constant, and its intercept) to be known in advance. A further example occurs in the derivation of the CTF friction law, i.e. a formula relating the friction coefficient to the value Re of the Reynolds number: such derivation, actively discussed in literature [7–10], is often based on assumptions about the shape of the mean velocity profile. A DNS, with its ability to evaluate the skin friction directly, and to plot the velocity profile in the law-of-the-wall form without implicit assumptions, is a poweful tool to complement experimental data in this research areas. Of course the main limitation of DNS lies in the limited values of the Reynolds number typically affordable in the numerical simulations. This is the reason why in this paper a method is developed with emphasis on computational efficiency.

A DNS at a relatively high value of Re will also offer the opportunity to observe to what extent a planar, pressure-driven and fully-developed turbulent flow (like a channel flow) presents analogies to the CTF. Besides direct curvature effects, which are not dominant in the present low-curvature geometry, a noticeable difference that could significantly affect the near-wall turbulence is the presence in the turbulent CTF of large-scale toroidal vortical structures. The laminar solution is known to be unstable above a well-defined (and curvature-dependent) critical value Re_c of the Reynolds number, above which such

structures, known as Taylor vortices, are quickly generated [11]. As Re increases further, the Taylor vortices undergo a series of transformations, after which they eventually reappear in the turbulent regime [12]. In his illuminated paper [13], Townsend surmised that turbulence in the CTF is basically of two different kinds, with one contribution from the wall shear and the other from the large-scale structures. DNS is the perfect tool to analyze the full flow field to the aim of revealing presence and characteristics of these large-scale structures, that are absent either in the plane channel and in the plane Couette flows.
The outline of the paper is as follows. In §2 the geometry of the problem and its numerical simulation will be presented, first by recalling in §2.1 the main ingredients of the method developed in Ref. [3], and then by describing its extension in §2.2. A validation of the computer code as well as a critical comparison of its results to available data will be given in §3, together with a quantitative assessment of its computational performance. Successively, in §4 the numerical simulation of the turbulent CTF will be described, with regards to discretization parameters and computational procedures. In §5 results will be presented in terms of averaged and instantaneous properties of the flow. Lastly, §6 will contain a conclusive summary.

2. Problem definition and numerical method

We consider a Taylor–Couette apparatus made by a moving inner cylinder, with radius $\mathcal{R}_i$ rotating at an angular velocity Ω_i, and a concentric, outer fixed cylinder with radius $\mathcal{R}_o$. In figure 1 the geometry employed in the present work is sketched: the radial coordinate is r, the axial and azimuthal coordinates being x and θ. The corresponding velocity components are v (wall-normal), u (spanwise) and w (streamwise). The amount of curvature is expressed by the geometric parameter $\zeta = \mathcal{R}_i/\mathcal{R}_o$. The Reynolds number Re is defined based on the inner cylinder rotating speed $W_i = \Omega_i \mathcal{R}_i$, the gap width $\mathcal{R}_o - \mathcal{R}_i = 2h$ between the two cylinders and the kinematic viscosity ν of the fluid. For a given value of ζ, when gravity and other external forces are neglected, Re becomes the sole relevant fluid dynamic parameter. Unless otherwise stated, the results presented in the following will be made non-dimensional by using W_i as reference velocity and h as reference length. When useful, the wall distance y will also be used, conveniently defined as $y = r - \mathcal{R}_i$ or $y = \mathcal{R}_o - r$. Quantities made non-dimensional in wall units will be indicated with a + superscript and will be computed with friction velocity u_τ (see §5 for details concerning its definition) and fluid viscosity ν.

2.1. *The starting point*

The Taylor–Couette system is of course most easily described in cylindrical coordinates. For cartesian coordinates, an effective and widely used formulation of the Navier–Stokes equations for the DNS of turbulent flows with two homogeneous directions was introduced by Kim, Moin & Moser [14], and is based on rewriting the equations of motion in terms of two scalar equations for the wall-normal components of the velocity and vorticity vector. A few studies have described its extension to a cylindrical geometry, to enjoy the same advantages: pressure is removed from the equations, and the resulting computational strategy is optimally fast when employed together with Fourier discretization in the

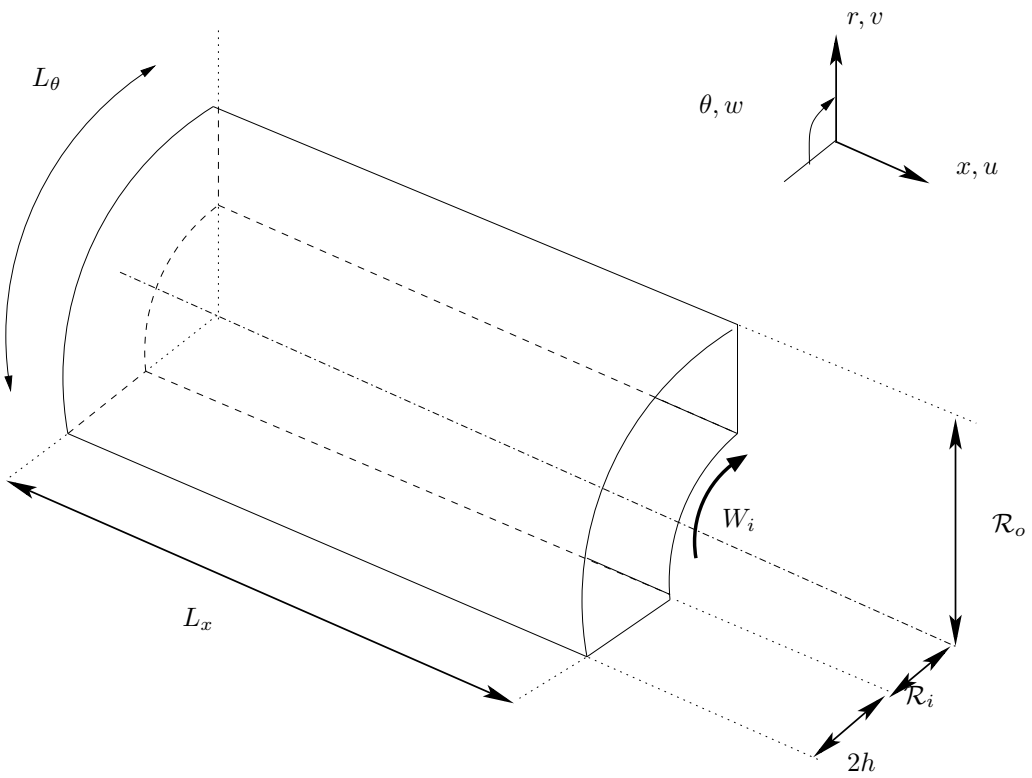

Fig. 1. Geometry of the Taylor–Couette flow system. The inner cylinder rotates at speed W_i and angolar velocity Ω_i, the outer cylinder is at rest.

homogeneous directions. We build for the present work upon the contribution by Quadrio & Luchini [3], who wrote evolutive equations for the radial components of velocity and vorticity in cylindrical coordinates, thus exporting to the cylindrical case the advantages and the computational efficiency of the cartesian one. The method by itself does not call for a particular discretization of the radial direction: in [3] finite difference were used, but spectral methods [15] and B-splines [16] have been tried too.

For completeness, we summarize here the main steps of the method described in [3] and used for the DNS of an annular pipe flow; then in §2.2 we describe the present extension to make it capable of turbulent TCF simulations.

Since two directions are homogeneous, the governing equations are first transformed in Fourier space. Fourier-transformed quantities will be denoted with a hat; α and m denote the axial and azimuthal wavenumbers, and $k^2 = \alpha^2 + m^2/r^2$. Note that k depends on the radial coordinate. In [3], after manipulation of the Navier–Stokes equations in primitive variables the following equation for the Fourier-transformed radial vorticity $\hat{\eta}$ was determined:

$$\frac{\partial \hat{\eta}}{\partial t} = \frac{1}{Re}\left(DD_*(\hat{\eta}) - k^2\hat{\eta} + 2\frac{im}{r^2}D(\hat{u}) + 2\frac{m\alpha}{r^2}\hat{v}\right) + \frac{im}{r}\widehat{HU} - i\alpha\widehat{HW} \quad (1)$$

In Eq. (1) the so-called Chandrasekar notation is employed for radial derivatives:

$$D(f) = \frac{\partial f}{\partial r}; \qquad D_*(f) = \frac{\partial f}{\partial r} + \frac{f}{r},$$

and $\widehat{HU}$, $\widehat{HW}$ and (in the following Eq.(2)) $\widehat{HV}$ denote the non-linear terms as written in the original primitive-variables equations.
After further manipulation, and leveraging the continuity equation, the temporal evolution of $\hat{v}$ was shown in [3] to be described by the following fourth-order differential equation:

$$\begin{aligned}\frac{\partial}{\partial t}\left[\hat{v} - D\left(\frac{1}{k^2}D_*(\hat{v})\right)\right] = \frac{1}{Re}D\left\{\frac{1}{k^2}\left[k^2 D_*(\hat{v}) - \right.\right. \\ \left.\left. D_* D D_*(\hat{v}) - 2\frac{m^2}{r^3}\hat{v} + 2\frac{im}{r^2}D(\hat{w}) - 2\frac{im}{r^3}\hat{w}\right]\right\} + \\ \frac{1}{Re}\left(-k^2\hat{v} + D D_*(\hat{v}) - 2\frac{im}{r^2}\hat{w}\right) + \\ D\left[\frac{1}{k^2}\left(i\alpha\,\widehat{HU} + \frac{im}{r}\widehat{HW}\right)\right] + \widehat{HV}. \quad (2)\end{aligned}$$

The differential system as a whole thus requires 6 boundary conditions; imposing the no-slip condition at both walls requires $\hat{v} = 0$, $D(\hat{v}) = 0$ and $\hat{\eta} = 0$ at the two walls $r = \mathcal{R}_i$ and $r = \mathcal{R}_o$ [17].
Even though evolution equations are written for $\hat{v}$ and $\hat{\eta}$ only, $\hat{u}$ and $\hat{w}$ velocity components are needed to advance the solution to the next time step, by computing the non-linear terms which are integrated esplicitely in time. The missing components are easily found by solving a 2×2 system made by the continuity equation and by the definition of $\hat{\eta}$. This differential system becomes algebraic when the present Fourier expansion is adopted.
Unlike the cartesian equations, viscous terms in Eqs. (1) and (2) contain terms in $\hat{u}$ and $\hat{w}$ too (which vanish in the planar limit $r \to \infty$), because of the Laplacian operator in cylindrical coordinates. Hence, when a partially-implicit procedure is used for temporal integration, these curvature-related viscous terms cannot be solved for implicitely. The solution adopted in [3] was to solve for them explicitely, since this was shown to imply no stability limitations.
The numerical method was of course spectral in the homogeneous directions, where – as usual in DNS spectral methods [18] – the non-linear terms are evaluated pseudo-spectrally to achieve good computational efficiency, thanks to the availability of Fast Fourier Transform algorithms. Radial derivatives were discretized in [3] with finite differences of second-order formal accuracy. The time integration was carried out with an explicit third-order Runge–Kutta method for the nonlinear terms and curvature-related viscous terms, and a second-order Crank–Nicholson scheme for the remaining viscous terms.

2.2. *The extension*

The numerical method described above needs to be improved further if a large-scale DNS of a turbulent flows at relatively high value of Re has to be performed. In particular the

second-order accuracy of the finite-difference schemes may not be considered satisfactory, and – most importantly – distributed-memory parallel computing capabilities are required.

The extension aims at replicating the strategy for efficient parallel computing that has been successfully implemented in our cartesian Navier–Stokes solver, recently described by Luchini and Quadrio in [4], and therefore only sketched here. In short, the key decision of discretizing the wall-normal derivatives with finite differences (FD) allows us to achieve high parallel performance and low communication requirements, thanks to the locality of the finite-difference operators. Data are partitioned among computing machines in wall-parallel slices, so that wall-parallel FFTs, needed to compute the non-linear terms with the pseudo-spectral approach, do not need inter-node communication. With a 5-point stencil for the FD discretization of radial derivatives, the implicit part of Eqns. (1) and (2) gives rise to pentadiagonal linear systems, one for each Fourier coefficient $\hat{\eta}$ and $\hat{v}$: their solution by a standard elimination algorithm proceeds via a first sweep of eliminations of the unknowns from one wall to the other, and then with a second sweep of backsubstitutions in the opposite direction. Since data are partitioned in wall-parallel slices, the solution of each system does require inter-node communication, and the computing machines can work one at a time only. However, the number of linear systems to be solved at each time step is very large, of the order of at least 10^4 in a typical turbulent channel flow DNS, and about 10^5 in the simulations described in the following. The solution of the linear systems can thus be efficiently carried out in parallel by using a pipelining strategy. In the Pipelined Linear Systems (PLS) method, a single machine is kept busy at working on the partial solution of many linear systems at once, while the companion machines are waited for transmitting back partial results of previous systems. Except for a startup and final phase, where pipelines are only partially filled, machines can thus work effectively in parallel most of the time. The global amount of data to be trasmitted across network with PLS is limited, thanks to the locality of FD operators in physical space: as an alternative, a fully spectral method would require the global transpose of the entire dataset, and this is known to carry a large networking load [19].

A FD discretization is more convenient than a spectral one in terms of parallel computing; its lesser spatial accuracy can be made comparable to that of spectral methods by using compact, high-accuracy FD schemes [20]. A further advantage is that the cost of dealing with compact schemes, that are usually implicit, can be further reduced for the Navier–Stokes equations: in the present context, they are made explicit by leveraging, as observed as early as in 1953 by Thomas [21], the lack of third derivatives in the governing equations. Reproducing the PLS approach of Ref. [4] in the cylindrical case, however, is not trivial. Both Eqs. (1) and (2) require further manipulation in order to arrive at a form where explicit compact schemes can be applied to the differential operators. If $a(r)$ indicates a generic r-dependent coefficient and f is the unknown function, terms in the form $a(r)D(f)$ do not lend themselves to a straightforward use of compact explicit schemes as in [4]. Such terms are thus rewritten after repeated integrations by parts, i.e. with substitutions of the type:

$$aD(f) = D(af) - D(a)f; \qquad aD_*(f) = D_*(af) - D(a)f. \tag{3}$$

Note that integrating by parts introduces additional known coefficients like $D(a)$, which depend on the radial coordinate (directly and/or via the wavenumbers): one of the sim-

plest among them in the actual equations is $D(1/k^2)$. Computing these known functions in the time-advancement loop takes a sizeable amount of computing time; alternatively they can be computed once at the beginning of the simulation and then stored, thus requiring a non-negligible amount of RAM. The choice between storing and computing on-the-fly depends of course on the available computational resources.
We refer the interested reader to Appendix A for additional details concerning the procedure of integration by parts, which leads to the final layout of the evolution equations. Though of complicated appeareance, they can be solved numerically by employing most of the numerical tools available for the cartesian case. Accordingly, the FD coefficients are determined following the procedure illustrated in Ref. [4]: a computational stencil made by 5 arbitrarily spaced (and smoothly strecthed) grid points is used to obtain a formal accuracy of order 4, and the coefficients are computed once and for all at the beginning of the simulation.

3. Validation

The present computer code is carefully validated against both numerical and experimental data available for CTF through preliminary calculations at non-turbulent values of Re.
The correctness and accuracy of finite-difference radial operators is preliminarly checked by computing the exact laminar solution. In the laminar regime, the flow is described by an exact solution of the Navier–Stokes equations [22]:

$$w(r) = \frac{W_i}{1-\zeta^2}\left[\frac{\mathcal{R}_i}{r} - \zeta^2 \frac{r}{\mathcal{R}_i}\right]. \tag{4}$$

Due to the term $\sim r^{-1}$, this solution cannot be represented exactly by the polinomial interpolation implied by a FD method. A discretization error is thus present, which is bound to decrease as the step size raised to the fourth power. The laminar velocity profile computed for $\zeta = 0.5$ is shown in Fig. 2 together with the analytical solution. The difference between computed and analytical curves is indeed observed to decrease as requested by the formal fourth-order accuracy of the numerical method.
The entire code is then tested both in large- and small-gap geometries for the first insurgence of Taylor vortices, to verify whether the evolution of small-amplitude disturbances is well represented. The curvature-dependent critical value Re_c of the Reynolds number, above which instability amplifies flow perturbations to develop Taylor vortices, is computed with the present code and compared to available data. For a given ζ, the code is thus run at various values of Re, starting from an initial condition made by the laminar solution with superimposed small-amplitude random disturbances. The discretization parameters are reported in table 1 ("straight-vortex" case). The temporal evolution of the kinetic energy is monitored, to verify whether the initial energy decreases or gets amplified depending on Re. For $\zeta = 0.5$ previous numerical simulations by Fasel & Booz [23], based on an axisymmetrical finite-difference method, determined $Re_c = 68.2$, whereas experimental measurements [24] indicated $Re_c = 68.4$. At the same curvature of $\zeta = 0.5$, we find Re_c to be confined within the range $68.2 < Re_c < 68.4$. For the small-gap case, at $\zeta = 0.95$ we compute $184 < Re_c < 186$, which agrees with the value of 185 determined by Moser et al. [25].

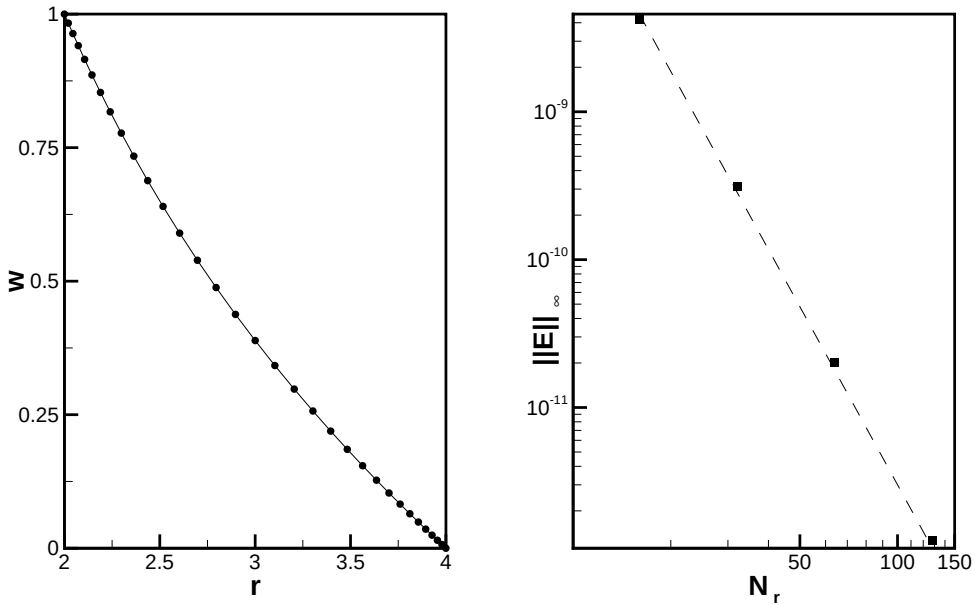

Fig. 2. Left: computed laminar velocity profile (symbols) and laminar analytical solution (4) (continuous line), for $\zeta = 0.5$ and $N_r = 32$ points in the radial direction. Right: difference $||E||_\infty$ between computed and analytical solutions, as a function of N_r. The straight line shows the expected decrease proportional to N_r^{-4}.

In the same flow regime, the torque needed to maintain the rotation of the inner cylinder is computed as an indicator of global spatial accuracy, and compared with previous works. The torque is defined as:

$$\mathcal{T} = \mu 2\pi \mathcal{R}_i^2 L \left(\left| \frac{\partial w}{\partial r} \right|_{r=\mathcal{R}_i} - \frac{w}{\mathcal{R}_i} \right). \tag{5}$$

where L is the axial length of the cylinders.
For the two cases at $\zeta = 0.5$ and $\zeta = 0.95$, table 2 show how values of $\mathcal{T}$ computed by the present code compare well (within small fractions of a percent) to literature data. XXX INCOMPLETE! XXX The difference between the torque evaluated at the inner and outer walls has been used in Ref. [23] to evaluate the adequacy of the spatial resolution employed in the simulations. In the present case, this difference is of 0.000109% only. When the number of points/modes are halved, it increases to 0.00242%, i.e. more than that required by the fourth-order accuracy of the radial derivative operators.
A further increase in Re brings us into the non-linear regime, where the straight Taylor vortices undergo a wavy azimuthal deformation and are named "wavy vortices" after the paper [26] by Coles. The prediction of quantitative properties of the wavy Taylor vortices, like their azimuthal wavenumber and their phase speed, allows a further confirmation of the present code. A simulation with the discretization parameters reported in table 1 ("wavy-vortex" case) has been carried out at $\zeta = 0.5$ and $Re = 250$. In this simulation

only, for comparison purposes the outer cylinder possesses a small amount of counter-rotation, such that Re based on the outer cylinder's rotation speed is $Re = -55$. The simulation, described in detail in [27], shows a pair of wavy vortices, with azimuthal wavenumber $m = 2$, and a characteristic rotation period $T = 117h/W_i$. This translates into a non-dimensional rotation speed $s = 2\pi/mT\Omega_i = 0.054$, which compares very well to the results presented by Snyder [28].

3.1. *Parallel performance*

The parallel performance of the code is documented for the problem size and on the computing system used for the turbulent simulation described later in §4.
The size of the computational problem is rather large, since we employ a spatial resolution of $N_\theta = 512$ and $N_z = 170$ Fourier modes in the azimuthal and axial directions respectively, while the number of points in the radial direction is set to $N_r = 129$. The simulation is carried out on a dedicated computing system, called a Personal Supercomputer, which is based on commodity personal computers. The special architecture of this system, that can be used with either the cartesian or the cylindrical code, is described in [4]. The system is made by 10 SMP nodes, each equipped with 2 Intel Xeon 2.66 GHz CPU, and at least 1GB of 266 MHz SDRAM. The nodes carry two Gigabit Ethnernet adapters each, and are connected in a ring topology. The low acquisition cost of this system allows us to use it in a dedicated mode for its entire lifespan.
On one Xeon CPU the code requires 680 MB of memory, and takes 182 seconds to compute a full time step for a 3-substeps Runge-Kutta temporal scheme. The amount of memory includes the storage space for the radial coefficients discussed in §2.2. Should RAM size become an issue, these coefficients can can be computed on-the-fly, thus saving 13% of RAM at the expense of a comparable increase in computing time. The CPU overhead of the cylindrical code compared to its cartesian counterpart is about 40% overall.
Figure 3 illustrates how the computation is speed up by employing an increasing number N of computing nodes. The ratio between the wall-clock time on one CPU and the wall clock time with N distributed-memory CPUs, i.e. the parallel speedup S, is plotted. The parallel speedup is not far from the linear one: the PLS parallel strategy in the present context thus exploits fully our low-cost computing system. The maximum measured speedup with $N = 10$ is about 9. The SMP capabilities of the nodes are then used on top of the distributed-memory parallel strategy. This allows a further 1.6 speedup factor from the use of 2 CPUs. The SMP speedup is additive to the distributed-memory speedup, and shows essentially no decrease with increasing the number of computing nodes. The entire wall clock time for the simulation described in §4 can thus be decreased from about 6 months to about 11 days when the entire system is used.
A further interesting observation that can be drawn from Fig.3 is the fact that the measured parallel performance is basically insensitive to the network bandwidth. When S is measured for parallel computations run between nodes for which the connecting network cards are slowed down from their native 1Gb/s bandwith to a bandwidth of 100Mb/s, essentially no penalty is observed. This reinforces the statement that the PLS parallel strategy effectively reduces the communication requirements.

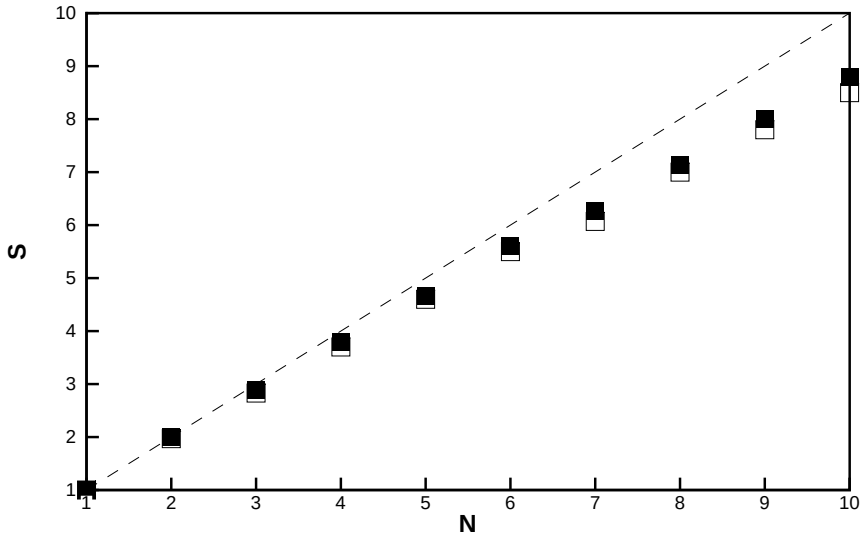

Fig. 3. Parallel speedup S of the code versus the number N of the computing nodes. Closed symbols are the measured speedup, and the dashed line represents linear speedup. Open symbols are the measured speedup when the network interface cards are slowed down from the usual 1Gb/s to 100Mb/s speed.

4. The turbulent Couette–Taylor flow simulations

The geometry considered in the present analysis is the small-gap geometry considered by Andereck, Liu & Swinney [5] with $\zeta = 0.882$, which gives $\mathcal{R}_i = 15h$ and $\mathcal{R}_o = 17h$. The value of the Reynolds number is set at $Re = 10500$, in order to obtain a value of the friction Reynolds number similar to $Re_\tau = 180$, which is typically considered the lowest value at which a turbulent channel flow presents a well-developed inner layer [14,29]. This represents a big computational challenge: for comparison, Bech et al. [30] computed a fully turbulent plane Couette flow, which is the limit for $\zeta \to 1$ of the present CTF, at $Re_\tau \approx 80$ only. According to Hamilton, Kim & Waleffe [31], the plane Couette flow is turbulent above $Re_\tau = 30$.

The size of the computational domain must be chosen by keeping in mind that periodic boundary conditions are used in the homogeneous directions: a periodic box imposes an artificial large-wavelength cutoff to the structures that can be represented in the numerical simulation. We set the axial wavelength at $L_z = 5h$: experimental results [12] indicate that $5h$ is indeed the wavelength of a pair of turbulent Taylor vortices, and is rather insensitive to the value of Re. The azimuthal extension of the box is set at $\ell_\theta = 5/8\pi$, which corresponds to a length $L_\theta = 10\pi h$ measured at the centerline of the gap.

The adequacy of the present size for the computational domain can be evaluated in terms of inner (viscous) units, i.e. by making lengths non-dimensional with the friction velocity u_τ (see later §5 for its definition) and the fluid viscosity. With the friction velocity computed at the inner wall $L_z^+ = 839$, whereas at the outer wall $L_z^+ = 946$. The

streamwise length is between $L_\theta^+ = 5576$ at the inner wall and $L_\theta^+ = 5600$ at the outer wall. A comparison with the domain sizes usually employed for DNS in the turbulent plane channel flow show that the domain size is adequate. The streamwise length L_θ^+ is 2.5 times the streamwise length typically employed [14] in the DNS of a plane turbulent channel flow at a comparable value of friction Reynolds number; the spanwise width, chosen to contain a single pair of large-scale vortices, is large enough to represent well the turbulent flow, being larger than that used in [29]. While the finite axial extent precludes describing possible long-range interactions between pairs of large-scale structures (as discussed in [23], such interactions can be neglected in a stability analysis of the CTF), the implied indefinite mirroring of periodic boxes makes the present simulation totally free from the end-effects that are unavoidable in laboratory experiments.
To obtain the resolution of all the significant spatial scales, $N_\theta = 512$ and $N_z = 170$ Fourier modes are used in the azimuthal and axial directions respectively, while the number of points in the radial direction is set to $N_r = 129$. The spatial resolution in wall units thus matches or exceeds the typical resolution employed in channel-flow DNS [29]. The global number of degrees of freedom amounts to $\approx 2.2 \cdot 10^7$. The parameters related to the spatial discretization are reported in table 3.
The resolution of the relevant temporal scales dictates the time step size. We use $\Delta t = 0.012\delta/W_i$, which is smaller than the stability limit of the employed Runge–Kutta scheme. In viscous units, this corresponds to $\Delta t^+ \approx 0.08$. A null mean pressure gradient is imposed in both the homogeneous directions.

4.1. *Computational procedures*

The initial condition for the simulations is based on the laminar solution (4); divergence-free velocity disturbances with amplitude $\mathcal{O}(10^{-4})$ and random phase are added to the whole set of Fourier modes. Different initial conditions have been considered in (less resolved) preliminary simulations, by either changing the amplitude of the disturbances, or by applying disturbances to a partial set of modes, or by starting the run from a null mean velocity profile instead of the profile (4). In terms of the long-time mean turbulent friction and others higher-order statistics, no difference has been noticed among these cases after the turbulent regime sets up, even though the time required to reach the statistically steady-state, as well as the behaviour of the flow during the initial transient, have been observed to depend on the details of the initial conditions.
The simulation is started from the above-described initial condition and let run for $1000\delta/W_i$. A flow field is stored on disk every 10 time units for later postprocessing. The size of a single flow field is 185 MBytes.
The time required for the simulation to settle to a statistically steady-state requires an initial time interval: we have estimated it based on the time history of various quantities, including the derivative of the space-mean velocity logitudinal velocity profile friction computed at the walls, which is related to Re_τ. Figure 4 shows how the length of this transient is about 150 time units. In computing statistical quantities, flow fields corresponding to the initial 300 time units are rejected.

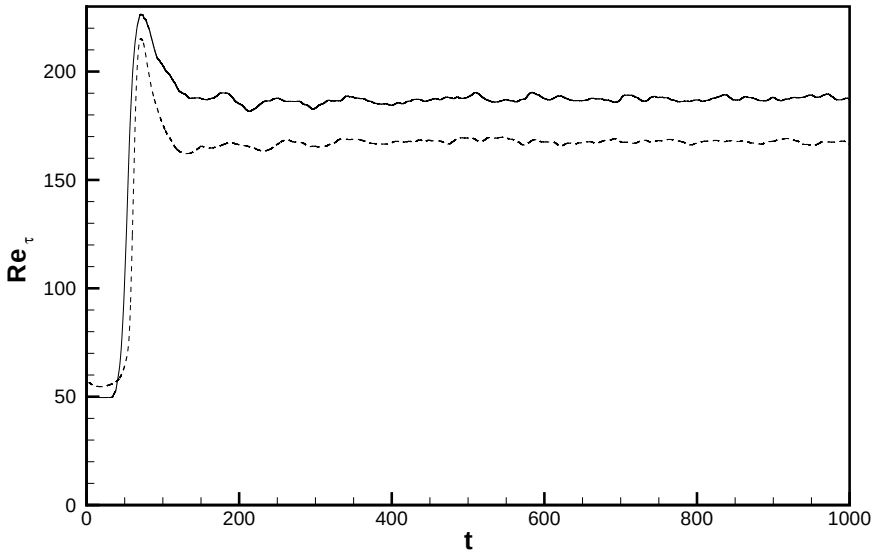

Fig. 4. Behaviour of Re_τ at the inner wall (continuous line) and outer wall (dashed line) as a function of time after the startup of the simulation.

5. Results

The first global flow feature that we consider is the mean friction. The shear-stress τ_w is computed for both the inner and the outer walls. Its mean value $\langle\tau_w\rangle$, averaged over time and over the homogeneous directions, allows us to compute a local friction velocity $u_\tau = \sqrt{\langle\tau_w\rangle/\rho}$ for each wall, from which a local Reynolds number $Re_\tau = u_\tau\delta/\nu$ can be obtained. The present results yield $Re_\tau = 189.3$ for the inner wall and $Re_\tau = 167.7$ for the outer wall. As a further confirmation of the adequacy of spatial resolution, we observe that the ratio between the values of Re_τ at the two walls equals ζ within 0.18%, which is certainly below the error implied by the temporal average of the fluctuating shear stress. The radial profile $\langle w\rangle$ of the mean azimuthal component of the velocity vector is shown in figure 5 and compared to the laminar solution (4). While the laminar profile at this curvature level is hardly distinguishable from a linear profile, the turbulent profile presents, in analogy to the plane turbulent Couette flow, two distinct regions: near the walls a shear-driven boundary layer, and in the central part of the gap a region where the velocity slowly decreases with r. In particular, the large central region presents an almost constant or very slowly-increasing angular momentum $r\langle w\rangle$; its value of nearly $0.5\mathcal{R}_i W_i$ agrees with the measurements by Taylor [11] and Smith & Townsend [32]. This property of the flow is seen here for the first time in a numerical simulation, and supports the hypothesis of a core region of constant angular momentum flow already put forward by Townsend [33].

In figure 6 the azimuthal velocity profile is plotted in semi-logarithmic scale and in local wall units against the wall distance y^+. Similarly to pressure-driven flows, a viscous

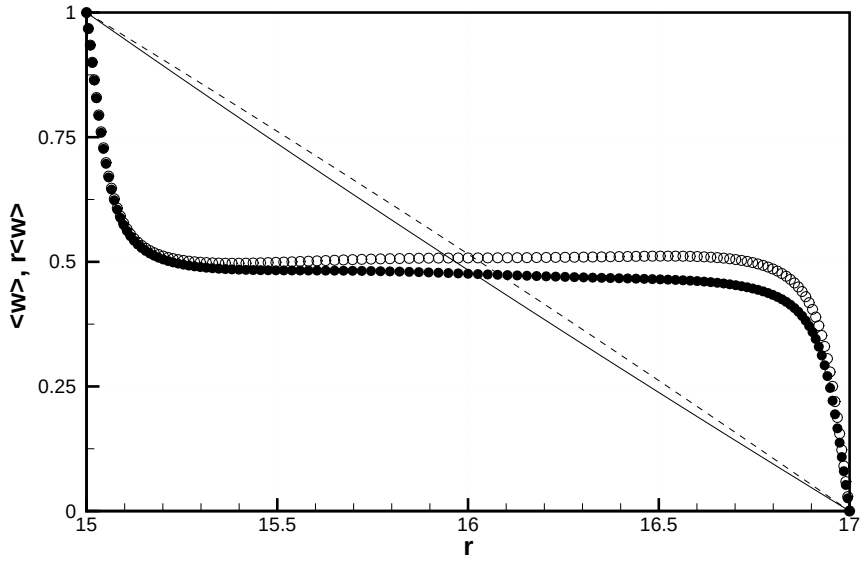

Fig. 5. Radial distribution of the mean azimuthal velocity $\langle w \rangle$ (closed symbols, continuous line) and of the angular momentum $r\langle w \rangle$ (open symbols, dashed line). Lines without symbols correspond to the analytical laminar solution. Angular momentum is made non-dimensional with $W_i \mathcal{R}_i$.

sublayer can be observed over both walls for $y^+ \lesssim 5$, where the profile follows the linear law $\langle w \rangle^+ = y^+$. The profiles over both walls are fairly similar up to $y^+ \approx 40$, but in the central part of the gap the outer profile becomes slightly higher than the inner one: this suggests that the friction velocity (local to each wall) is not the correct scaling velocity in this region of the flow.

The very existence of a logarithmic layer, where the mean velocity profile is described by:

$$\langle w \rangle^+ = \frac{1}{\kappa} \ln y^+ + B,$$

as well as its characterization through the numerical values of the von Kármán constant κ and the intercept B, are matters where scholars have not yet agreed upon [6]. Figure 7 shows the azimuthal mean velocity profile, plotted in law-of-the-wall form for the inner wall only. The computed profile is compared to a few laws proposed in the literature. In particular for a plane Couette flow at $Re_\tau = 82.2$ the values $1/\kappa = 2.55$ and $B = 4.7$ have been proposed [30], whereas for the same flow at $Re_\tau = 52$ the values $1/\kappa = 2.5$ and $B = 4.6$ have been used [34]. The values for the plane channel flow at $Re_\tau = 180$, after Kim, Moin & Moser [14], are $1/\kappa = 2.5$ and $B = 5.5$.

Figure 7 reveals a rather limited extent of the logarithmic region, the relatively high value of Re notwithstanding. (A rough estimate is that the present profile has constant slope for $20 \lesssim y^+ \lesssim 40$. The outer edge of the logarithmic layer can also be estimated from figure 6 as the position where the curves relative to the two walls start to diverge. On the contrary, the profile of the plane channel flow has constant slope in a range of nearly

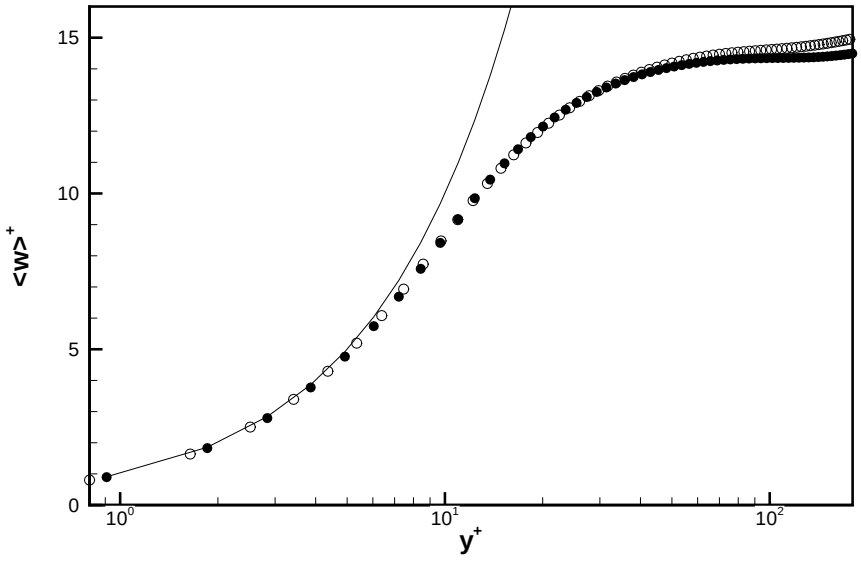

Fig. 6. Mean azimuthal velocity profile $\langle w \rangle^+$, in local wall units, over the inner wall (closed symbols) and the outer wall (open symbols). The continuous line is the linear profile $\langle w \rangle^+ = y^+$.

100 wall units.) The values of $1/\kappa$ and B from the plane channel case do not provide a good fit, whereas the ones from the plane Couette flow appear more suited to the present velocity profile. The best fitting line seems to be that by [30]. The main information that can be drawn is thus to reinforce the statement by Smith & Townsend [32]: "no significant region of logarithmic variation of velocity can exist" for "any flow of Reynolds number less than 20000" in a Taylor–Couette flow with the outer cylinder at rest. According to a semi-empirical law [35], which relates the outer-scale Reynolds number to Re_τ, this corresponds to $Re_\tau \approx 340$. As long as such information is not available, the collected evidence suggests that, at least for these relatively low values of Re, κ should take values equal or slightly reduced compared to the plane channel flow. We recall however that curvature for the considered geometry at $\zeta = 0.882$ is rather weak.

The observed shape of the mean velocity profile is relevant to the ongoing discussion about the derivation of a friction law for the turbulent Couette–Taylor flow. In recent years, Lathrop et al [7] derived an approximate friction law based on the assumption of a logarithmic velocity profile, whereas Panton [8] started from the assumption that the core region has constant angular momentum. The present results, which show to a very good approximation the presence of the constant angular momentum region, appear to lend more support to the latter assumption, tough wider logarithmic layers could develop at higher Re.

The variance of the velocity fluctuations are plotted in figure 8 across the whole gap. One observes high levels of fluctuations for the streamwise component, which is also the one with more marked asimmetry between the two walls and shows higher turbulence activity over the outer wall. The radial component peaks at the centerline with a symmetric

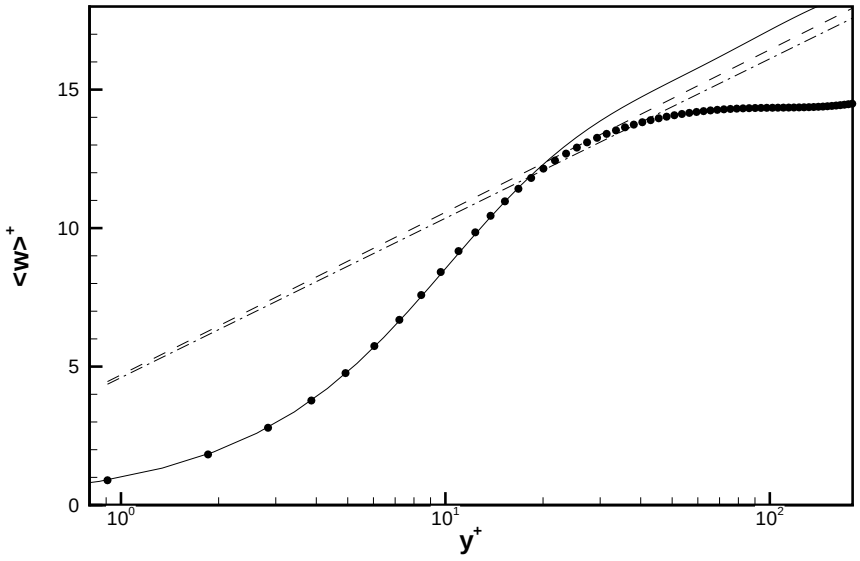

Fig. 7. Mean azimuthal velocity profile $\langle w \rangle^+$ (symbols) over the inner wall, compared with logarithmic laws proposed in literature. Dashed line: plane Couette flow at $Re_\tau = 52$ by [30]. Dotted line: plane Couette flow at $Re_\tau = 82.2$ by [34]. Continuous line: profile for plane channel flow at $Re_\tau = 180$ by [29].

profile, whereas the spanwise component is nearly symmetric and remarkably intense.
A better look can be obtained by plotting the root-mean-square values for both walls in local wall units against y^+ in figure 9, thus implicitely accounting for the different values of the friction Reynolds number. Convex and concave walls do still present discernible differences: in particular the turbulence activity as deduced by the level of streamwise velocity fluctuations is still larger over the outer wall. A similar but less pronounced behaviour is observed for the spanwise component. Inner scaling seems to work for the radial component, at least very near the wall: when the centerline is approached, the two profiles over the inner and outer wall appear to diverge. We interpret the failure of friction velocity in scaling the r.m.s. profiles as an effect of the turbulent Taylor vortices. Near the wall they induce perturbations in the u and w components without affecting v, because of the impermeability constraint. In a sense, these perturbations behave similarly to the so-called inactive motions hypothesized by Townsend [33] to populate the turbulent boundary layer, and known to be responsible for the so-called anomalous scaling [36,37]. Figure 9 reports also the r.m.s. value of velocity fluctuations for the plane channel flow, taken from [29]. The streamwise component is quite similar, while the wall-normal component is similar in the near-wall region only. The spanwise component in the channel flow presents a much lower level of activity, and is thus the component where the contribution by the turbulent Taylor vortices is the most relevant. Figure 10 gives a qualitative picture of the whole flow field. The turbulent Taylor vortices can be clearly observed. In laboratory experiments, one often has to resort to passive tracers to visualize these large-scale structures, whereas DNS makes the flow variables

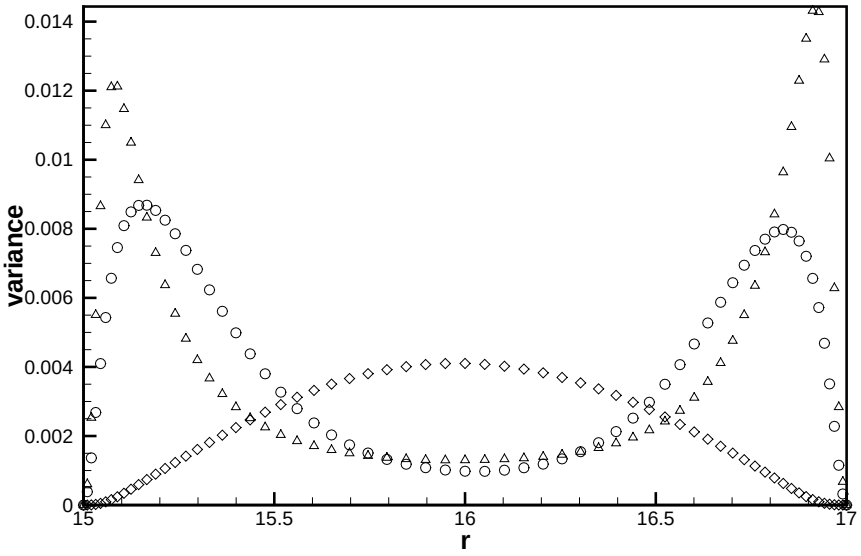

Fig. 8. Variance of velocity fluctuations across the gap. Triangles: streamwise component. Diamonds: wall-normal component. Circles: spanwise component. For clarity only one every two points is shown.

easily available. In Fig.10 the large-scale structures are indeed cleary recognizable based on actual flow variables. In the figure the entire computational domain is visualized, represented in cartesian coordinates and made rectilinear along the azimuthal direction for clarity sake. The two isosurfaces represent values of $\pm 0.12 W_i$ for the radial velocity component, and emphasize the presence of two large-scale roll-like structures. It is evident how the vortices are strongly modulated by the noisy turbulent background, so that their boundary is somewhat blurried. They are however clearly identifiable, and extend their influcence down to the wall.

6. Discussion and conclusions

A direct numerical simulations of a Taylor–Couette flow in the fully turbulent regime has been presented. The value of the Reynolds number – up to $Re_\tau \approx 190$ based on friction velocity, viscosity of the fluid and half gap width – is high enough to compare turbulent statistics to the ones of planar pressure-driven flows.

Such a demanding simulation has required developing a numerical method designed *ad hoc*. It discretizes the governing equations with high accuracy and exploits the computing power of a parallel computing system, which is assembled from commodity hardware. The code, based on Fourier expansion in the homogeneous directions and on fourth-order, compact finite differences in the radial direction, has been validated by computing several physical quantities available from previous DNS or experiments in the laminar and transitional regimes, and has then made possible the first DNS of the Couette–Taylor flow in the fully turbulent regime.

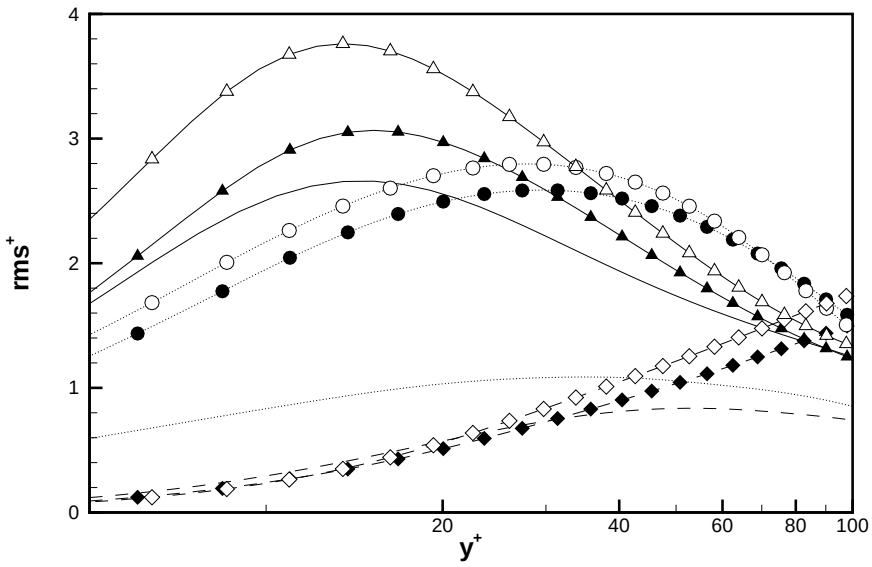

Fig. 9. Root-mean-square value of velocity fluctuations above both walls. Closed symbols: inner wall. Open symbols: outer wall. Lines without symbols: plane channel flow at $Re_\tau = 180$ by [14]. Triangles and continuous line: streamwise component. Diamond and dashed line: wall-normal component. Circles and dotted line: spanwise component. For clarity only one every two points is shown.

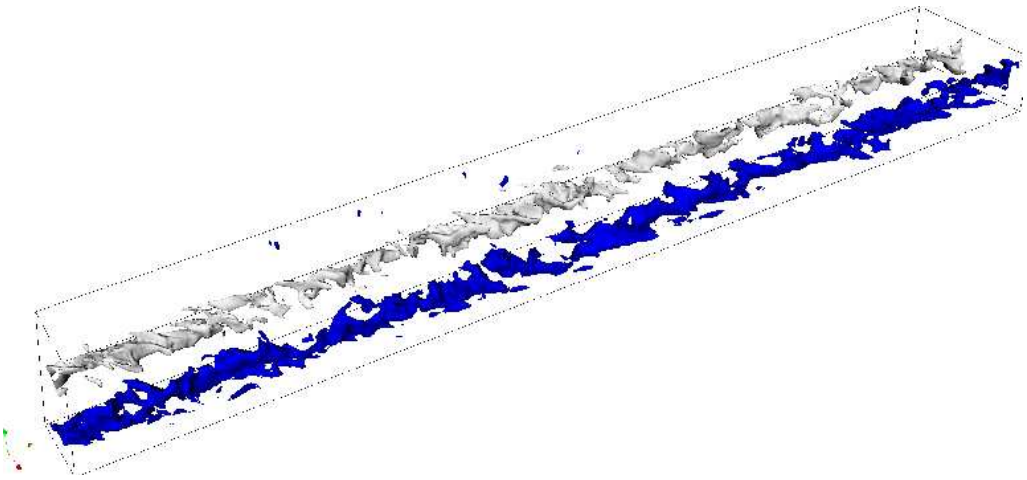

Fig. 10. Snapshot of an instantaneous flow field. For clarity, the azimuthal axis is made rectilinear, so that the computational domain is deformed into a rectangular box. The bottom wall moves from left to right. Isosurfaces for the radial velocity component are shown, at levels of $\pm 0.12 W_i$: negative levels are in light gray, and positive in dark gray.

A geometry with relatively small curvature has been considered. In comparing statistics to other wall turbulent flows, analogies and differences have been discussed, the main source for the latter being the presence of the curvature-induced turbulent Taylor vortices. The mean velocity profile does not exhibit an equilibrium logarithmic region at the present value of Re, contrasting the pressure-driven flows. A core region with almost constant angular momentum has been revealed by our simulations, and the numerical value of this constant compares very well to experimental observations taken at different Re. The analysis of the root-mean-square values of velocity fluctuations, in comparison with the ones from a plane channel flow, reveals the lack of inner scaling, and suggests the existence of different contributing physical processes.

Two distinct sources of turbulence fluctuations can indeed be identified in the present flow: (i) the large-scale vortices, generated by an instability mechanism, and (ii) the wall turbulence cycle, related to the near-wall shear, which in the present context produces small-scale fluctuations and provides a noisy background for the vortices. A visualization of a snapshots of the flow field has shown how the large-scale structures retain their basic shape while embedded in the flow, though blurried by the surrounding small-scale turbulence. The interaction of the small-scale turbulence with the large-scale structures, and the possibility of discerning and eventually separating their contributions to the flow statistics is an interesting long-term objective on which we are currently working.

References

[1] R. Tagg, The Couette-Taylor problem, Non Linear Science Today 4 (3) (1994) 1–25.

[2] D. Haim, L. M. Pismen, Performance of a photochemical reactor in the regime of the Taylor-Görtler vortical flow, Chem. Eng. Sc. 49 (8) (1994) 1119–1129.

[3] M. Quadrio, P. Luchini, Direct numerical simulation of the turbulent flow in a pipe with annular cross-section, Eur. J. Mech. B / Fluids 21 (2002) 413–427.

[4] P. Luchini, M. Quadrio, A low-cost parallel implementation of direct numerical simulation of wall turbulence, J. Comp. Phys. 211 (2) (2006) 551–571.
URL `file:///home/mq/Library/luchini-quadrio-2006.pdf`

[5] C. D. Andereck, S. S. Liu, H. L. Swinney, Flow regimes in a circular Couette system with indipendently rotating cylinders, J. Fluid Mech. 164 (1986) 155–183.

[6] V. Patel, F. Sotiropolous, Longitudinal curvature effects in turbulent boundary layers, Prog. Aerospace Sci. 33 (1997) 1–70.

[7] D. P. Lathrop, J. Fineberg, H. L. Swinney, Transition to shear-driven turbulence in Couette-Taylor flow, Phys. Rev. A 46 (1992) 6390–6405.

[8] R. L. Panton, Scaling laws for the angular momentum of a completely turbulent Couette flow, C. R. Acad. Sci. Paris, II 315 (1992) 1467–1473.

[9] G. Lewis, H. Swinney, Velocity structure functions, scaling and transitions in high-Reynolds-number Couette-Taylor flow, Phys. Rev. E 59 (5) (1999) 5457–4567.
URL `file:///home/mq/Library/lewis-swinney-1999.pdf`

[10] B. Eckhardt, S. Grossmann, D. Lohse, Scaling of global momentum transport in Taylor-Couette and pipe flow.
URL `file:///home/mq/Library/eckhardt-grossmann-lohse-2000.pdf`

[11] G. I. Taylor, Fluid Friction Between Rotating Cylinders, 1- Torque Measurements, Proc. Roy. Soc., Ser. A 157 (1936) 546.

[12] E. L. Koschmieder, Turbulent Taylor vortex flow, J. Fluid Mech. 93 (1979) 515–527.

[13] A. A. Townsend, Axisymmetric Couette flow at large Taylor numbers, J. Fluid Mech. 144 (1984) 329–362.

[14] J. Kim, P. Moin, R. Moser, Turbulence statistics in fully developed channel flow at low Reynolds number, J. Fluid Mech. 177 (1987) 133–166.

[15] J. C. Neves, P. Moin, R. D. Moser, Effects of convex transverse curvature on wall-bounded turbulence. Part 1. The velocity and vorticity, J. Fluid Mech. 272 (1994) 349–381.

[16] W. Kwok, R. Moser, J. Jiménez, A critical evaluation of the resolution properties of B-spline and compact finite difference methods, J. Comp. Phys. 174 (2001) 510–551.

[17] S. Orszag, M. Israeli, M. Deville, Boundary Conditions for Incompressible Flows, J. Sci. Comp. 1 (1) (1986) 75–111.

[18] R. Rogallo, Numerical Experiments in Homogeneous Turbulence, TM 81315, NASA (1981).

[19] R. B. Pelz, The Parallel Fourier Pseudospectral Method, J. Comp. Phys. 92 (1991) 296–312.

[20] S. Lele, Compact Finite Difference Schemes with Spectral-like Resolution, J. Comp. Phys. 103 (1992) 16–42.

[21] L. Thomas, The stability of plane Poiseuille flow, Phys. Rev. 91 (4) (1953) 780–783.

[22] G. K. Batchelor, An Introduction to Fluid Dynamics, Cambridge University Press, 1967.

[23] H. Fasel, O. Booz, Numerical investigation of supercritical Taylor-vortex flow for a wide gap, J. Fluid Mech. 138 (1984) 21–52.

[24] A. Schultz, G. Pfister, Bifurcation and structure of flow between counter-rotating cylinders, Lecture Notes in Physics 549 (2000) 37–54.

[25] R. Moser, P. Moin, A. Leonard, A spectral numerical method for the Navier–Stokes equations with application to Taylor-Couette flow, J. Comp. Phys. 52 (1983) 524–544.

[26] D. Coles, Transition in circular Couette flow, J. Fluid Mech. 21 (1965) 385–425.

[27] D. Pirrò, Flow on streamwise-curved surfaces: forced transition and turbulence, Ph.D. thesis, Politecnico di Milano (2005).

[28] H. A. Snyder, Change in wave-form and mean flow associated with wavelength variations in rotating Couette flow. Part 1, J. Fluid Mech. 35 (1969) 337–352.

[29] R. Moser, J. Kim, N. Mansour, Direct numerical simulation of turbulent channel flow up to $Re_\theta = 590$, Phys. Fluids 11 (4) (1999) 943–945.

[30] K. Bech, N. Tillmark, P. Alfredsson, H. Andresson, An investigation of turbulent plane Couette flow at low Reynolds numbers, J. Fluid Mech. 286 (1995) 291–325.

[31] J. Hamilton, J. Kim, F. Waleffe, Regeneration mechanisms of near-wall turbulence structures, J. Fluid Mech. 287 (1995) 317–348.

[32] G. P. Smith, A. A. Townsend, Turbulent Couette flow between concentric cylinders at large Taylor numbers, J. Fluid Mech. 123 (1982) 187–217.

[33] A. Townsend, The structure of turbulent shear flows, 2nd Edition, Cambridge University Press, 1976.

[34] J. Komminaho, A. Lundbladh, A. Johansson, Very large structures in plane turbulent Couette flow, J. Fluid Mech. 320 (1996) 259–285.

[35] E. Bilgen, R. Boulos, Functional dependence of torque coefficient of coaxial cylinders on gap width and Reynolds numbers, Transaction ASME J. Fluids Eng. 95 (1973) 122–126.

[36] D. De Graaf, J. Eaton, Reynolds-number scaling of the flat-plate turbulent boundary layer, J. Fluid Mech. 422 (2000) 319–346.

[37] J. Del Álamo, J. Jiménez, P. Zandonade, R. Moser, Scaling of the energy spectra of turbulent channels, J. Fluid Mech. 500 (2004) 135–144.
URL `file:///home/mq/Library/delalamo-etal-2004.pdf`

[38] M. Quadrio, P. Luchini, The numerical solution of the incompressible Navier–Stokes equations in cartesian and cylindrical geometries on a low-cost, dedicated parallel computer., Dip. Ing. Aerospaziale, Politecnico di Milano DIA-SR 04-16.
URL `http://pc-quadrio.aero.polimi.it/papers/2004-DIA0416.pdf`

Acknowledgments

We acknowledge financial support by the Italian Ministry of University and Research through the PRIN project 2004 on *Turbulent flows over curved walls.*

Appendix

This Appendix presents additional details concerning the entire procedure of extending the numerical method from what published in [3] to the one employed in the present simulations. The complete derivation can be found in Refs. [38] and [27].
To arrive at the form of the governing equation which is discretized in the computer code, we begin by eliminating third derivatives in Eq. (2) via the continuity equation. The simple substituion:

$$D_*(\hat{v}) = -i\alpha\hat{u} - \frac{im}{r}\hat{w}.$$

works around the difficulty of deriving explict compact schemes along the Thomas' strategy [21], which is designed for the Orr-Sommerfeld equation where third derivatives are missing. Of course a few viscous terms have to be moved into the part of the evolution equation (2) that is to be integrated explicitely in time, thus creating potential stability problem. This price however has been paid already when transforming the equations (in cylindrical coordinates) from the primitive variables to the velocity-vorticity formulation. *A posteriori* we determined empirically that these terms do not imply temporal stability limitations, and the choice of the time step size is still limited by temporal accuracy considerations. Of course the problem could get worse as long as the degree of curvature is increased.
The procedure of repeated integrations by parts needed to massage Eqns. (1) and (2) into a form suitable for the application of the compact finite-difference operators is described now with some detail.
In Eqn. (2), the first term which is integrated by parts following (3) is the time derivative, which becomes:

$$\frac{\partial}{\partial t}\left[-D\left(\frac{1}{k^2}D_*(\hat{v})\right)\right] = \frac{\partial}{\partial t}\left[-DD_*\left(\frac{1}{k^2}\hat{v}\right) + D\left(D(\frac{1}{k^2})\right)\hat{v}\right].$$

In the righ-hand-side of Eqn. (2), perhaps the most complicated term is:

$$D\left[\frac{1}{k^2}\left(-D_*DD_*\hat{v}\right)\right],$$

where first the continuity equation must be invoked to cancel the third derivative. Repeated integrations by parts then allow the r-dependent coefficients to remain only in the innermost positions. After some algebra, the result is:

$$\begin{aligned} -D\left[\frac{1}{k^2}\left(D_*DD_*\hat{v}\right)\right] &= -DD_*DD_*\left(\frac{1}{k^2}\hat{v}\right) + D\left[\frac{1}{r}DD\left(\frac{1}{k^2}\hat{v}\right)\right] + \\ &- 2DD_*\left[\frac{1}{r}D\left(\frac{1}{k^2}\right)\hat{v}\right] + D\left[DDD\left(\frac{1}{k^2}\right)\hat{v}\right] - D\left[\frac{1}{r^2}D\left(\frac{1}{k^2}\right)\hat{v}\right] + \\ &- 3DD_*\left[D\left(\frac{1}{k^2}\right)\left(i\alpha\hat{u} + \frac{im}{r}\hat{w}\right)\right]. \end{aligned}$$

As a result of the use of the continuity equation, the last term has appeared which cannot be solved for implicitly, and must thus join the viscous curvature terms in the explicit part.
The last term of Eqn. (2) which needs manipulation is:

$$D\left[\frac{1}{k^2}\left(2\frac{im}{r^2}D(\hat{w})\right)\right] = 2im\left\{DD\left(\frac{\hat{w}}{k^2r^2}\right) - D\left[\frac{1}{r^2}D\left(\frac{1}{k^2}\right)\hat{w}\right] + D\left(\frac{2}{k^2r^3}\hat{w}\right)\right\}.$$

The same sequence of integration by parts must be carried out for Eqn. (1) for the radial vorticity, arriving at the following substitution:

$$2\frac{im}{r}D(\hat{u}) = 2im\left[D\left(\frac{u}{r^2}\right) + 2\frac{u}{r^3}\right].$$

Lastly, the nonlinear terms too contain radial derivatives, and some terms therein must be integrated by parts.

This procedure leads to the final, rather long form of the equations for $\hat{v}$ and $\hat{\eta}$, which lends itself to a discretization in the radial direction with explicit compact finite difference schemes of fourth-order accuracy over a five point stencil. It is written here in full for completness, without time discretization for notational simplicity:

$$\begin{aligned}
&\frac{\partial}{\partial t}\left[\hat{v} - DD_*\left(\frac{1}{k^2}\hat{v}\right) + D\left(\hat{v}D(\frac{1}{k^2})\right)\right] = \\
&\frac{1}{Re}\left\{2DD_*(\hat{v}) - DD_*DD_*\left(\frac{1}{k^2}\hat{v}\right) + D\left[\frac{1}{r}DD\left(\frac{1}{k^2}\right)\hat{v}\right] - 2DD_*\left[\frac{1}{r}D\left(\frac{1}{k^2}\right)\hat{v}\right] + \right. \\
&\quad +D\left[DDD\left(\frac{1}{k^2}\right)\hat{v}\right] - D\left[\frac{1}{r^2}D_1\left(\frac{1}{k^2}\right)\hat{v}\right] - 3DD_*\left[D\left(\frac{1}{k^2}\right)\left(i\alpha\hat{u} + \frac{im}{r}\hat{w}\right)\right] + \\
&\quad -2m^2D\left(\frac{1}{k^2r^2}\hat{v}\right) + imD\left[\frac{1}{k^2r^2}\hat{w}\right] + 2im\left[DD\left(\frac{1}{k^2r^2}\hat{w}\right) - D\left[\frac{1}{r^2}D\left(\frac{1}{k^2}\right)\hat{w}\right]\right] + \\
&\quad \left. -k^2\hat{v} - 2\frac{im}{r^2}\hat{w}\right\} - i\alpha\left[DD_*\left(\frac{1}{k^2}\widehat{uv}\right) - D\left(D\left(\frac{1}{k^2}\widehat{uv}\right)\right)\right] - im\left[DD\left(\frac{1}{rk^2}\widehat{vw}\right) + \\
&\quad +3D\left(\frac{1}{r^2k^2}\widehat{vw}\right) - D\left(\frac{1}{r}D\left(\frac{1}{k^2}\right)\widehat{vw}\right)\right] + D\left[\frac{1}{k^2}\left(\alpha^2\hat{u}^2 + 2\frac{\alpha m}{r}\widehat{uw} + \frac{m^2}{r^2}\hat{w}^2\right)\right] + \\
&\qquad\qquad - i\alpha\widehat{uv} - D(\hat{v}^2) - \frac{im}{r}\widehat{vw} - \frac{1}{r}\hat{v}^2 + \frac{1}{r}\hat{w}^2; \quad (6)
\end{aligned}$$

$$\begin{aligned}
\frac{\partial\hat{\eta}}{\partial t} = \frac{1}{Re}&\left\{DD_*(\hat{\eta}) - k^2\hat{\eta} + 2im\left[D\left(\frac{1}{r^2}\hat{u}\right) + 2\frac{\hat{u}}{r^3} - \frac{i\alpha}{r^2}\hat{v}\right]\right\} - im\left[\frac{i\alpha}{r}\hat{u}^2 + \right. \\
&\left. D\left(\frac{\widehat{uv}}{r}\right) + \frac{2}{r^2}\widehat{uv} + \frac{im}{r^2}\widehat{uw}\right] + i\alpha\left[i\alpha\widehat{uw} + D\left(\widehat{vw}\right) + \frac{im}{r}\hat{w}^2 + \frac{2}{r}\widehat{vw}\right]. \quad (7)
\end{aligned}$$

	L_x	L_θ	N_x	N_r	N_θ	Re
"straight-vortex" case	$4h$	πh	64	64	32	60-190
"wavy-vortex" case	$4h$	$2\pi h$	64	64	32	255

Table 1
Size of the computational domain and grid resolution for the preliminary simulations in the "straight-vortex" and "wavy-vortex" regimes (see text).

Re	here	$\zeta = 0.5$ [23]
60.0	16.7551	16.7551
68.0	16.7551	16.7551
70.0	17.1542	17.1537
75.0	18.1634	18.1627
80.0	19.0536	19.0527

Table 2
Comparison between the value of the torque $\mathcal{T}$ computed by the present code and: (left) [23] for $\zeta = 0.5$; (right) [25] for $\zeta = 0.95$.

Position	L_z	L_θ	L_z^+	L_θ^+	Δz^+	y^+	$(r\Delta\theta)^+$
inner wall	$5h$	$9.37\pi h$	946	5576	5.6	0.9	10.9
centreline	$5h$	$10\pi h$	889	5588	5.2	4.6	10.9
outer wall	$5h$	$10.62\pi h$	839	5600	4.9	0.8	10.9

Table 3
Size of the computational domain and grid resolution for the turbulent Couette–Taylor simulation. Wall units are computed on the basis of the friction velocity relative to each wall, as defined in §5.